

RADIO CONTINUUM STUDY OF THE LARGE MAGELLANIC CLOUD SUPERNOVA REMNANT HONEYCOMB NEBULA

R. Z. E. Alsaberi¹, M. D. Filipović¹, H. Sano^{2,3}, P. Kavanagh⁴, P. Janas⁴,
J. L. Payne¹ and D. Urošević⁵

¹ Western Sydney University, Locked Bag 1797, Penrith South DC, NSW 1797, Australia
E-mail: 19158264@student.westernsydney.edu.au

² Faculty of Engineering, Gifu University, 1-1 Yanagido, Gifu 501-1193, Japan

³ Center for Space Research and Utilization Promotion (c-SRUP), Gifu University,
1-1 Yanagido, Gifu 501-1193, Japan

⁴ Department of Experimental Physics, Maynooth University, Maynooth, Co. Kildare, Ireland

⁵ Department of Astronomy, Faculty of Mathematics, University of Belgrade,
Studentski trg 16, 11000 Belgrade, Serbia

(Received: January 9, 2024; Accepted: February 18, 2024)

SUMMARY: We present the first and deepest Australia Telescope Compact Array radio continuum images of the Honeycomb Nebula at 2000 and 5500 MHz solely from archival data. The resolutions of these images are $3.6 \times 2.8 \text{ arcsec}^2$ and $1.3 \times 1.2 \text{ arcsec}^2$ at 2000 and 5500 MHz. We find an average radio spectral index for the remnant of -0.76 ± 0.07 . Polarisation maps at 5500 MHz reveal an average fractional polarisation of $25 \pm 5\%$ with a maximum value of 95 ± 16 . We estimate the equipartition field for Honeycomb Nebula of $48 \pm 5 \mu\text{G}$, with an estimated minimum energy of $E_{\min} = 3 \times 10^{49} \text{ erg}$. The estimated surface brightness, $\Sigma_{1 \text{ GHz}}$, is $30 \times 10^{-20} \text{ W m}^{-2} \text{ Hz}^{-1} \text{ sr}^{-1}$; applying the Σ -D relation suggests this supernova remnant is expanding into a low-density environment. Finally, using H α data, we can support the idea that the Honeycomb Nebula exploded inside a low-density wind cavity. We suggest that this remnant is likely to be between late free expansion stage and early Sedov phase of evolution and expanding into a low-density medium.

Key words. ISM: planetary nebulae: individual: Honeycomb nebula – Methods: observational – Radio continuum: ISM – Magellanic Clouds

1. INTRODUCTION

Supernova Remnants (SNRs) play an essential role in galaxies, enriching the Interstellar Medium (ISM) producing a significant impact on their structure and physical properties. However, the study of

SNRs within our own Galaxy is not ideal because of a high level of dust and gas absorption, compounding the difficulties of achieving accurate distance measurements. Instead, we look to nearby galaxies, such as the Large Magellanic Cloud (LMC), located at a known distance of $\sim 50 \text{ kpc}$ (Macri et al. 2006, Pietrzyński et al. 2019). This allows observers to assume all objects within the galaxy are located at the same distance, making physical measurements, including the extent of physical size, more reliable. Additionally, the LMC is approximately face-on in

© 2024 The Author(s). Published by Astronomical Observatory of Belgrade and Faculty of Mathematics, University of Belgrade. This open access article is distributed under CC BY-NC-ND 4.0 International licence.

orientation (having an inclination angle of $\sim 35^\circ$, van der Marel and Cioni 2001) and is near enough to allow deep, high-resolution (spatial and spectral) multi-frequency SNR observations (Maggi *et al.* 2016, Bozzetto *et al.* 2017, Yew *et al.* 2021, Bozzetto *et al.* 2023).

The Honeycomb Nebula (MC SNRJ0535–6918) is one of the most peculiar SNRs in the LMC – just a few arcminutes south-east of the well-known SN 1987A. It was discovered by Wang (1992) using the *ROSAT* survey. Meaburn *et al.* (1993) presented a kinematic study of the Honeycomb Nebula and concluded that all the kinematic features can be generated as one or more young SNRs colliding in a dense environment. Chu *et al.* (1995) used a combination of archival and new *ROSAT* X-ray data and Australia Telescope Compact Array (ATCA) with Molonglo Observatory Synthesis Telescope (MOST) radio data to find both bright X-ray and nonthermal radio emission. Moreover, they reported an enhanced [S II]/H α ratio and a steep radio spectral index of -1.2 . Redman *et al.* (1999) used optical observations obtained from the *Manchester Echelle* spectrometer to produce new kinematical and density data for the Honeycomb Nebula. Meaburn *et al.* (2010) also used optical data in a spectral analysis of forbidden line ratios to infer the nebula is most likely a SNR.

Meaburn *et al.* (2010) found Honeycomb Nebula to be more extended in soft X-ray emission and possibly could be a small section on the edge of a giant LMC shell. They suggest that a secondary supernova explosion on this edge may be responsible for the creation of the nebula.

In this paper, we present a radio continuum study of the Honeycomb Nebula using ATCA archival data to produce high-fidelity images and we compare them with other multiwavelength data (X-ray and optical). In Section 2 we present the data used and their reduction details. Section 3 explores further analysis and discussion including radio morphology, polarisation, spectral index, surface brightness and luminosity. Finally, in Section 4, we conclude with a summary of our findings.

2. DATA

2.1. Radio continuum observations

The Honeycomb Nebula has been serendipity observed with ATCA, due to its location in the field of view of SN 1987A (Chu *et al.* 1995). Archival¹ ATCA observations, including observing dates, project numbers, observation frequency and time spent on source and array configurations are presented in Table 1. All observations were carried out in ‘snap-shot’ mode, with 1-hour of integration over a 12-hour period as a

minimum. All used the Compact Array Broadband Backend with 2048 MHz bandwidth, centred at wavelengths of 6 cm ($\nu = 4500$ –6500 MHz; the midpoint at 5500 MHz) and 13 cm ($\nu = 1972$ and 2150 MHz).

We used MIRIAD² (Sault *et al.* 1995), KARMA³ (Gooch 1995), and DS9⁴ (Joye and Mandel 2003) software packages for reduction and analysis. All observations were calibrated using the phase and flux calibrators listed in Table 1 with three rounds of phase-only self-calibration using the SELFCAL task. Imaging was completed using the multi-frequency synthesis INVERT task with uniform Briggs weighting (robust = 0) and a beam size of $1.3 \times 1.2 \text{ arcsec}^2$ for 5500 MHz (see Fig. 1-top). We combined 2150 and 1972 MHz data to produce one image at 2000 MHz with a beam size of $3.6 \times 2.8 \text{ arcsec}^2$ (see Fig. 1-bottom). The MFCLEAN and RESTOR algorithms were used to deconvolve the images, with primary beam correction applied using the LINMOS task. We follow the same process with stokes Q and U parameters to produce polarisation maps with a beam size of $3 \times 3 \text{ arcsec}^2$ (see Fig. 2 and Section 3.3 for more details).

2.2. HI observations

To better understand the interstellar environment surrounding the Honeycomb Nebula, we used archived HI data from the ATCA & Parkes 64-m radio telescope (Kim *et al.* 2003). The combined HI data has an angular resolution of $\sim 60''$, corresponding to a spatial resolution of ~ 15 pc. Typical noise fluctuations are ~ 0.3 K at a velocity resolution of $\sim 1.6 \text{ km s}^{-1}$ (Fig. 3).

2.3. X-ray observations

Detailed comparisons of X-ray morphology with our new radio images were made using sub-arcsecond resolution data from the *Chandra* X-ray Observatory (Weisskopf *et al.* 1996). Due to its proximity to SN 1987A, the Honeycomb Nebula has been observed many times by *Chandra*. We retrieved all available data that included the Honeycomb Nebula using the Advanced CCD Imaging Spectrometer S-array (ACIS-S, Garmire *et al.* 2003) with exposure times of $\gtrsim 40$ ks. A list of observations is given in Table 2.

We processed each of these datasets using the CIAO v4.15⁵ (Fruscione *et al.* 2006) software pack-

²<http://www.atnf.csiro.au/computing/software/miriad/>

³<http://www.atnf.csiro.au/computing/software/karma/>

⁴<https://sites.google.com/cfa.harvard.edu/saoimageds9>

⁵See <http://cxc.harvard.edu/ciao/>

¹Australia Telescope Online Archive (ATOA), hosted by the Australia Telescope National Facility (ATNF): <https://atoa.atnf.csiro.au>

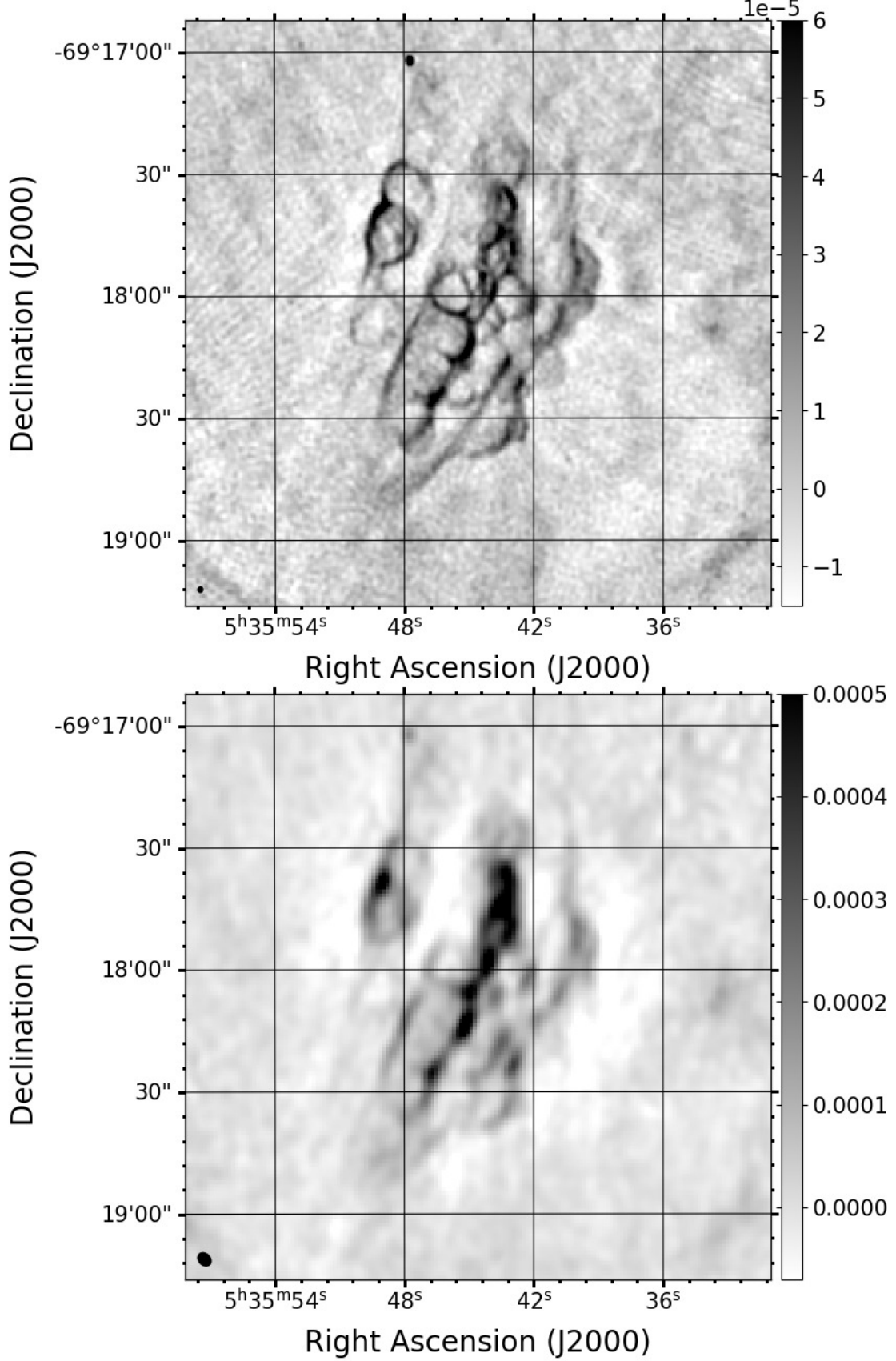


Fig. 1: ATCA intensity images of the Honeycomb Nebula at 5500 MHz (top) and 2000 MHz (bottom). The ellipses at the bottom left corner represent a synthesised beam of $1.3 \times 1.2 \text{ arcsec}^2$ and $3.6 \times 2.8 \text{ arcsec}^2$ for 5500 and 2000 MHz, respectively. The colour bars on the right-hand side represent intensity gradients in Jy beam^{-1} .

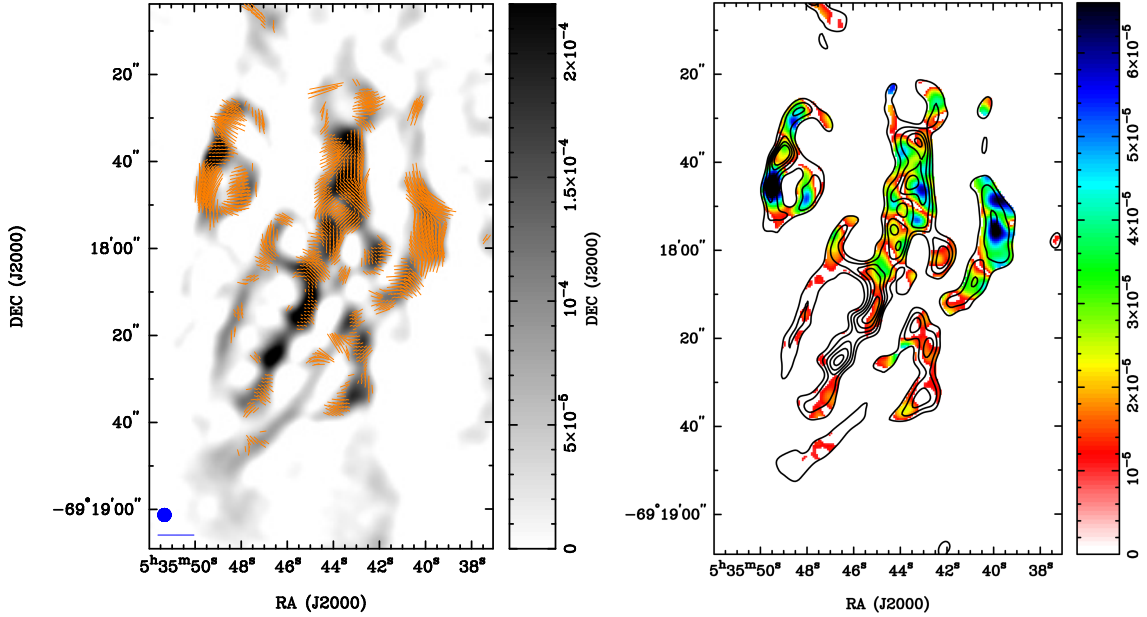


Fig. 2: Fractional Polarisation vectors of the Honeycomb Nebula overlaid on the ATCA intensity image at 5500 MHz (left). The blue circle at the lower left corner represents a synthesised beam of 5×5 arcsec and the blue line below represents the 100 per cent polarisation. The bar on the right-hand side represents grey scale intensity gradients in Jy beam^{-1} . The polarisation intensity map of the Honeycomb Nebula at 5500 MHz (right) with intensity contour lines overlaid. The contour levels are 0.00005 , 0.0001 , 0.00015 , 0.0002 , and $0.00025 \text{ Jy beam}^{-1}$. The colour bar on the right represent gradients of polarisation intensity.

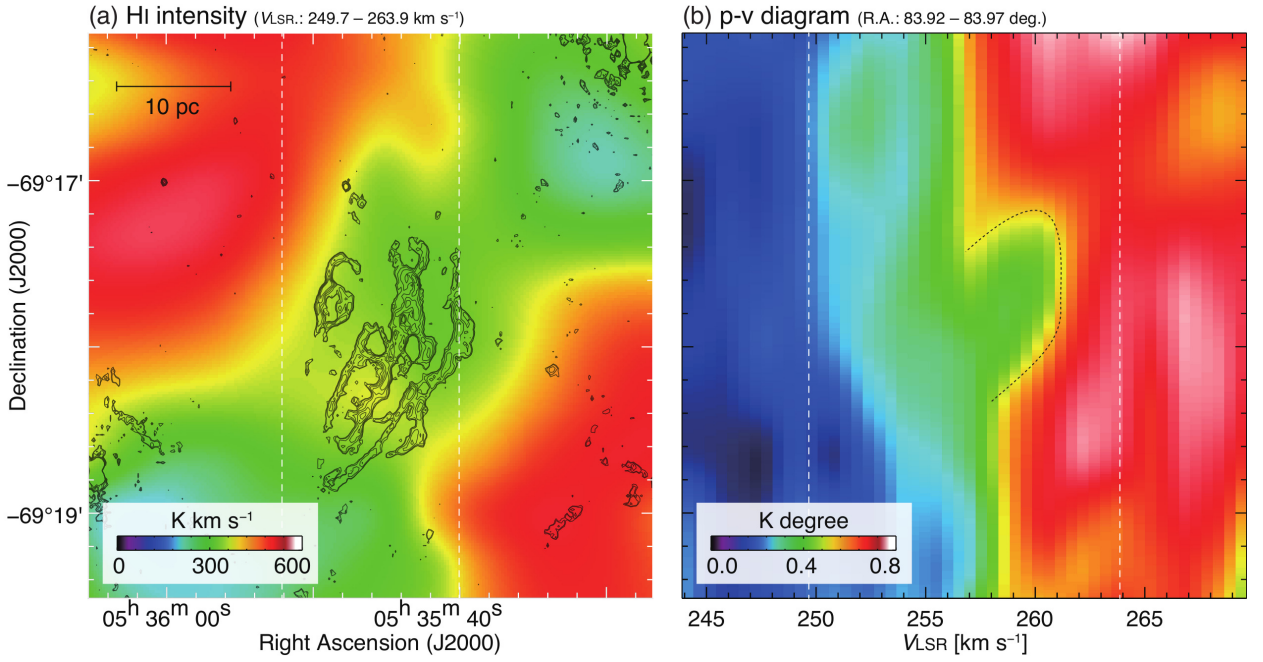


Fig. 3: (a) Velocity integrated Parkes HI intensity map from 249.7 to 263.9 km s^{-1} superposed with ATCA 5500 MHz intensity contours. Contour levels are 1.0 , 1.2 , 1.8 , 2.8 , 4.2 , and $6.0 \times 10^{-5} \text{ Jy beam}^{-1}$. (b) HI position-velocity (p-v) diagram having an integration range from RA 83.92 to 83.97 degrees. The dashed curve indicates the boundary of a HI hollowed-out structure.

age with CALDB v4.10.7⁶. The data were reduced using the contributed script `chandra_repro`, resulting in the filtered exposure times listed in Table 2.

We reprojected the resulting level 2 event files from each observation to a common tangent point using CIAO `reproject_obs` before merging them using `merge_obs` for a combined exposure time of ~ 382 ks. Finally, flux images were produced from the merged event file at 0.5–1 keV, 1–2 keV and 2–8 keV using `fluximage`. The resulting three-colour image is shown in Fig. 4.

2.4. Optical observations

HST images of the Honeycomb Nebula were downloaded from the Mikulski Archive for Space Telescopes⁷. We used SWARP⁸ (Bertin et al. 2002) to stitch four images together to produce a single image (Fig. 5). We also use the H α +[N II] image of the Honeycomb Nebula from Meaburn et al. (2010) (Fig. 6) for comparison.

3. RESULTS AND DISCUSSION

3.1. Radio morphology

In Fig. 1, we present deep high-resolution radio-continuum images of the Honeycomb Nebula at 5500 and 2000 MHz. Its radio emission is primarily non-thermal, based on a steep spectral index (see Section 3.2). The east and south-east parts of the remnant appears as if a blast wave expanded into a rarefied environment and then collided with nearby dense gas (Meaburn et al. 1993). Its mid-section is bright, as especially noted in the 2000 MHz image (Fig. 1-bottom). Using our images, we calculated the centre of the Honeycomb Nebula at RA (J2000) = $5^h35^m45.16^s$, Dec (J2000) = $-69^\circ17'59''95$ with a size of $\sim 59 \times 35$ arcsec 2 ($\sim 14 \times 8$ pc).

To better understand the morphology of the SNR, we compare our new 5500 MHz ATCA image with HST and *Chandra* images as shown in Fig. 5. We note the radio emission follows the optical emission somewhat (see Fig. 5(b), but there is no correlation with the X-ray emission, which we believe is predominantly thermal (Fig. 5(c)). The west and south-west side of the remnant disappear in the H α +[N II] image (Fig. 6) which support heterogeneous densities as noted in the blast wave propagation scenario stated above.

Perhaps most similar to the morphology of the Honeycomb Nebula is MCSNR J0052–7236 (DEM S68) in the Small Magellanic Cloud, which is

significantly larger with a diameter of 88 pc. Additional information can be found in Filipović et al. (2005), Payne et al. (2007), Filipović et al. (2008), Owen et al. (2011), Haberl et al. (2012), Crawford et al. (2014), Roper et al. (2015), Alsaberi et al. (2019), Gvaramadze et al. (2019), Maggi et al. (2019), Joseph et al. (2019) and Cotton et al. (2024).

3.2. Spectral index

The radio spectral index α can be defined as the slope in power-law dependence of flux density S_ν on frequency ν : $S_\nu \propto \nu^\alpha$. We produced a spectral index map for the Honeycomb Nebula with the 2000 and 5500 MHz images (Fig. 7) by first re-gridding the images to the finest pixel size (0.4×0.4 arcsec 2) using the MIRIAD task REGRID. These were then smoothed to a common resolution (4×4 arcsec 2) using CONVOL, after which the task MATHS created the spectral index map (Fig. 7) in a similar way as LMC MCSNR 0624–6948 (Filipović et al. 2022). The spectral index values for the west and southwest sides of the remnant are changing from -0.5 to 0.5 , while the east, northeast and main body show steep values (<-0.5). Interestingly, we notice a very steep region (-1.5) towards the north (see Fig. 7).

In Fig. 8, we plot integrated flux densities at three frequencies in order to estimate the Honeycomb Nebula's overall spectral index. Our observations were combined with flux density measurements from ASKAP (Pennock et al. 2021) (see Table 3). We acknowledge errors are introduced when measuring ATCA flux densities because of missing short spacing inherent in the data. In the figure, the black line represents the best power-law weighted least-squares fit wherein we find a spatially integrated spectral index of $\langle \alpha \rangle = -0.76 \pm 0.07$, flatter than a previous estimation of -1.2 (Chu et al. 1995). This may be indicative of a younger-aged SNR as our value is steeper than average shell-type SNRs, as observed for the Galaxy and a range of nearby galaxies, including the LMC (Reynolds et al. 2012, Urošević 2014, Galvin and Filipović 2014, Maggi et al. 2019, Filipović and Tothill 2021, Bozzetto et al. 2017, 2023). Although there are regions with $\alpha > 0$, this strongly indicates that non-thermal radio emission dominates across the SNR.

3.3. Polarisation

Fractional polarisation (P) can be calculated using the equation:

$$P = \frac{\sqrt{S_Q^2 + S_U^2}}{S_I}, \quad (1)$$

where P is the mean fractional polarisation, S_Q , S_U , and S_I are intensities for the Q , U , and I Stokes parameters, respectively.

⁶See <http://cxc.harvard.edu/caldb/>

⁷<https://mast.stsci.edu/portal/Mashup/Clients/Mast/Portal.html>

⁸<https://www.astromatic.net/software/swarp/>

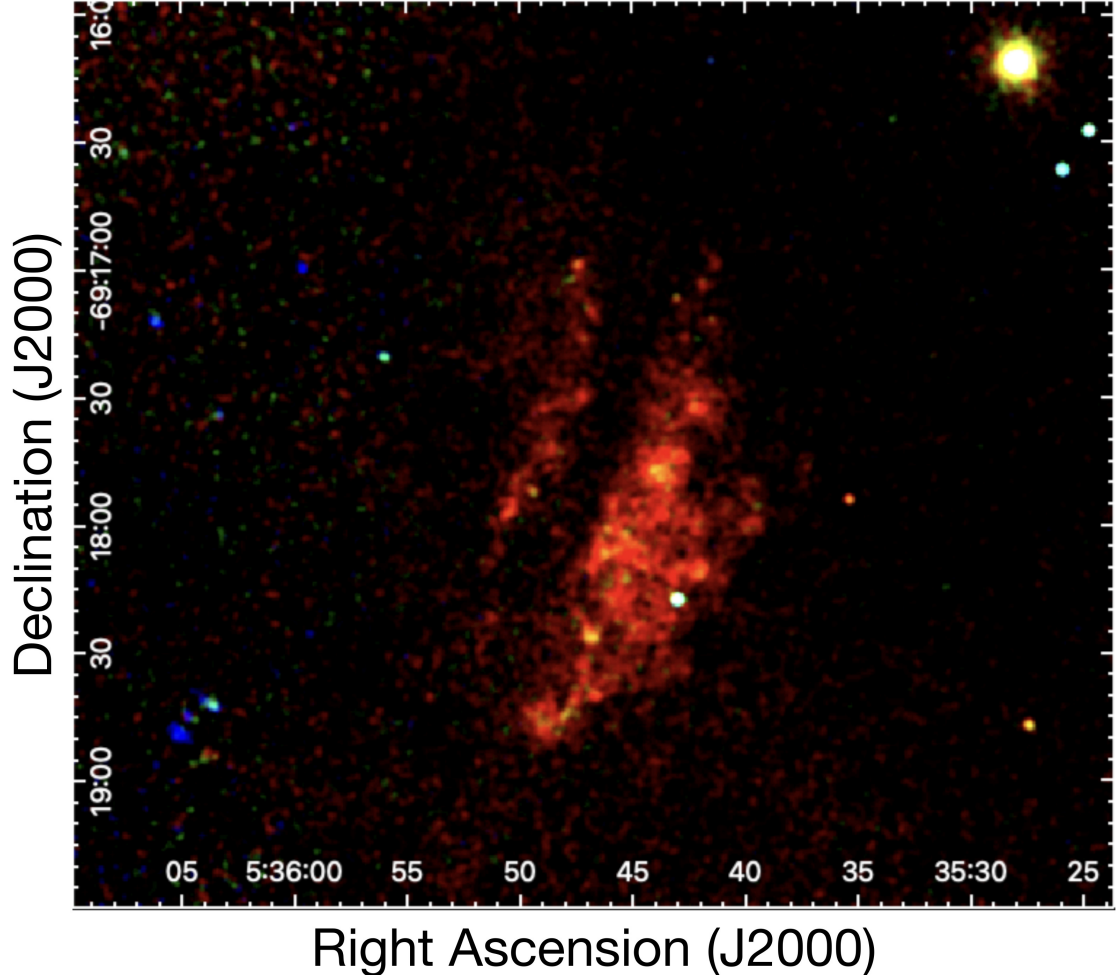


Fig. 4: Three-colour *Chandra* image of the Honeycomb Nebula. RGB colours are 0.5–1 keV, 1–2 keV, and 2–8 keV. The image has been smoothed using a 3×3 pixel Gaussian kernel. SN 1987A is the bright source in the top-right of the image.

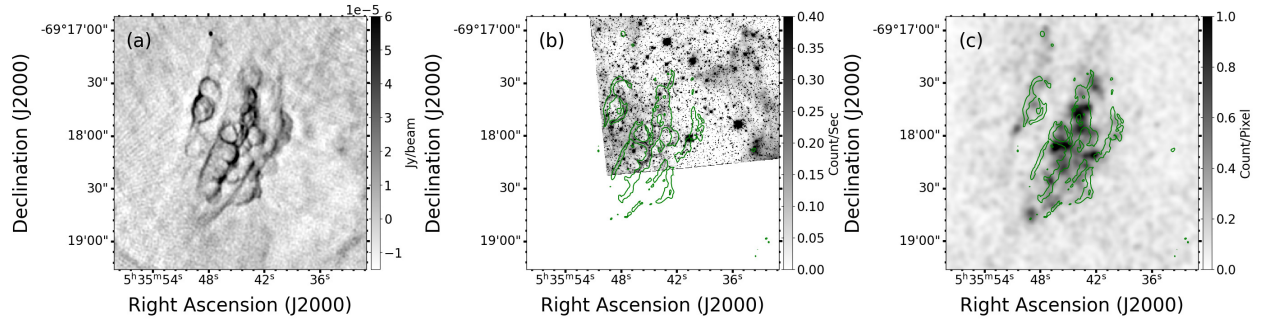


Fig. 5: Honeycomb Nebula: a) our new ATCA image at 5500 MHz, b) partial HST image, and c) smoothed *Chandra* (0.5–1 keV) image. Green contours are from the 5500 MHz image at $20 \mu\text{Jy}$.

We used the MIRIAD task IMPOL to produce polarisation maps for the Honeycomb Nebula. We find the fractional polarisation is generally in the radial direction and prominent in the east, west, and mid-section of the remnant (Fig. 2). Its average P value at 5500 MHz is $24 \pm 5\%$ with a maximum value of $95 \pm 16\%$.

3.4. Equipartition model

There are three standard ways to determine the magnetic field strength in the ISM: from the Zeeman splitting, rotation measure, and by using the so-called equipartition calculation (eqp). The Zeeman splitting method is only applicable to very dense phases of ISM, like cores of molecular clouds. Rotation mea-

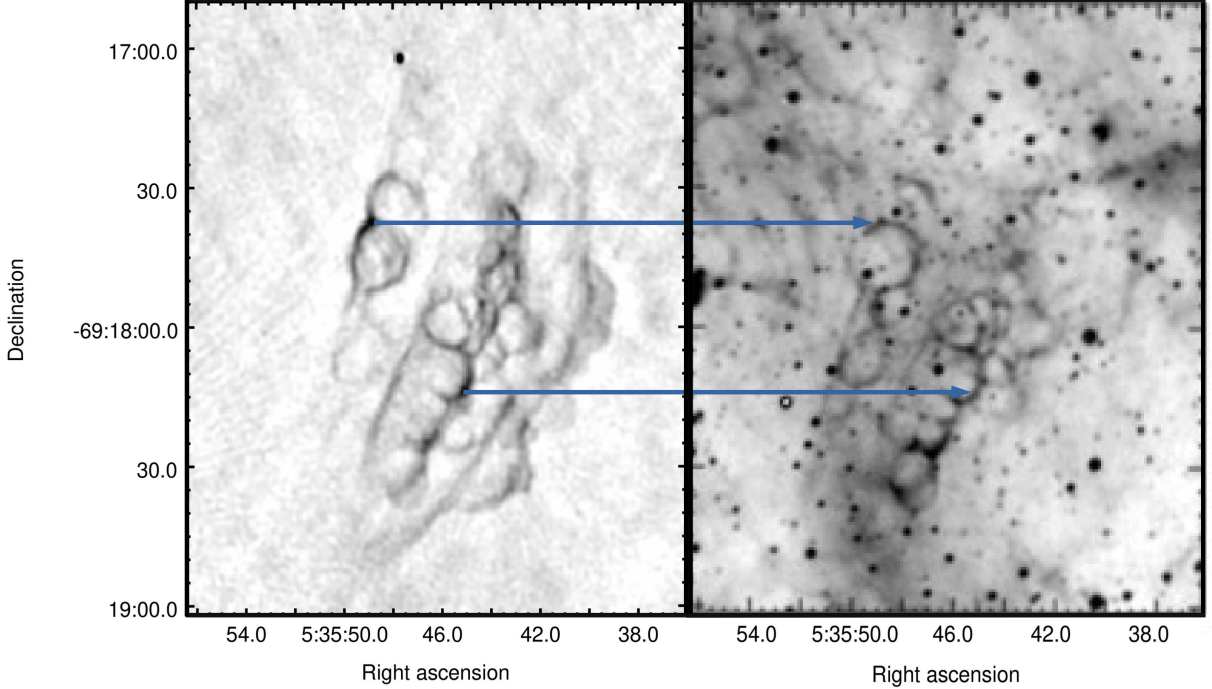


Fig. 6: ATCA image of the Honeycomb Nebula at 5500 MHz (left) with corresponding regions in the H α +[N II] image (right) from Meaburn et al. (2010). Note the west and south-west regions of the remnant seem to disappear in the H α +[N II] image.

sure method is based on polarisation of radio emission from radio sources. The eqp method assumes equipartition, i.e. equal partition between the cosmic rays (CRs) and magnetic field energy densities.

To estimate the magnetic field, we used eqp model⁹. This method uses modeling and simple parameters to estimate intrinsic magnetic field strength and energy contained in the magnetic field and cosmic ray particles using radio synchrotron emission (Arbutina et al. 2012, 2013, Urošević et al. 2018).

This approach is a purely analytical, described as a rough, only an order of magnitude estimate, due to assumptions used in analytical derivations, and errors in determination of distance, angular diameter, spectral index, filling factor, and flux density, tailored especially for the magnetic field strength in SNRs. Arbutina et al. (2012, 2013), Urošević et al. (2018) present two models; the difference is in assumption whether there is eqp, precisely constant partition with CRs or only CR electrons. Urošević et al. (2018) showed the latter type of eqp is a better assumption to the former.

Using the Urošević et al. (2018) model¹⁰, the mean eqp field over the whole Honeycomb Nebula is $48 \pm 5 \mu\text{G}$, with an estimated minimum energy of $E_{\min} = 3 \times 10^{49} \text{ erg}$. As this SNR is young and

expanding into a low-density environment (see Section 3.7), the magnetic field has to be amplified, not only compressed by shock wave. (The original model, cited in Arbutina et al. (2012), yields a mean eqp field of $80 \pm 5 \mu\text{G}$, with an estimated minimum energy of $E_{\min} = 9 \times 10^{49} \text{ erg}$.)

3.5. HI distribution

Fig. 3(a) shows the integrated intensity map of HI towards the Honeycomb Nebula. There is an intensity gradient of HI increasing from the centre of the SNR to the north-east and south-west. The brightest feature ($\sim 600 \text{ K km s}^{-1}$) is roughly twice higher than the lowest towards the SNR ($\sim 300 \text{ K km s}^{-1}$). On the other hand, the north-west and south-west regions show the lowest HI values ($\sim 200\text{--}300 \text{ K km s}^{-1}$); roughly consistent with the direction of the SNR.

Fig. 3(b) shows the position–velocity diagram of HI towards the Honeycomb Nebula. We find the HI intensity is hollowed out along the dashed curve, the velocity range of which is from 257 to 262 km s^{-1} . Moreover, the spatial extent of hollowed-out HI is roughly consistent with the radio size of the SNR. We argue these hollowed-out distributions of HI indicate an expanding gas motion from stellar winds originating with the progenitor system. The expanding velocity of HI in the Honeycomb Nebula is estimated to be $\Delta V \sim 5 \text{ km s}^{-1}$, which is roughly similar to Magellanic SNRs RX J0046.5–7308 ($\Delta V \sim 3\text{--}5 \text{ km s}^{-1}$ Sano et al. 2019) and N132D ($\Delta V \sim 6 \text{ km s}^{-1}$ Sano

⁹<http://poincare.matf.bg.ac.rs/~arbo/eqp>

¹⁰We use: $\alpha = 0.76$, $\theta = 1.22 \text{ arcmin}$, $\kappa = 0$, $S_{5500 \text{ MHz}} = 0.046 \text{ Jy}$, and $f = 0.25$.

Table 1: A summary of ATCA observations used in this study.

Date	Project Code	Array Configuration	No. Channels	Bandwidth ν (MHz)	Frequency ν (MHz)	Phase Calibrator	Flux Calibrator	Integrated time (minutes)
10 Apr 2010	C015	6A	2048	2048	2150	PKS B0530–727	PKS B1934–638	103.2
10 Apr 2010	C015	6A	2048	2048	5500	PKS B0530–727	PKS B1934–638	187.8
11 Apr 2010	C015	6A	2048	2048	5500	PKS B0530–727	PKS B1934–638	491.4
27 Jun 2010	C015	6C	2048	2048	1972,2150	PKS B0530–727	PKS B1934–638	73.8
27 Jun 2010	C015	6C	2048	2048	5500	PKS B0530–727	PKS B1934–638	118.2
10 Jul 2010	C015	1.5C	2048	2048	5500	PKS B0530–727	PKS B1934–638	118.2
19 Nov 2010	C015	6A	2048	2048	2150	PKS B0530–727	PKS B1934–638	108
19 Nov 2010	C015	6A	2048	2048	5500	PKS B0530–727	PKS B1934–638	105
22 Jan 2011	C015	6A	2048	2048	2150	PKS B0530–727	PKS B1934–638	162.6
22 Jan 2011	C015	6A	2048	2048	5500	PKS B0530–727	PKS B1934–638	162.6
25 Jan 2011	C015	6A	2048	2048	5500	PKS B0530–727	PKS B1934–638	475.2
20 Mar 2011	C015	1.5A	2048	2048	2150	PKS B0530–727	PKS B1934–638	132.6
20 Mar 2011	C015	1.5A	2048	2048	5500	PKS B0530–727	PKS B1934–638	123.6
22 Apr 2011	C015	6A	2048	2048	5500	PKS B0530–727	PKS B1934–638	469.8
23 Apr 2011	C015	6A	2048	2048	1972,2150	PKS B0530–727	PKS B1934–638	133.2
23 Apr 2011	C015	6A	2048	2048	5500	PKS B0530–727	PKS B1934–638	133.2
27 Aug 2011	C015	6B	2048	2048	1972	PKS B0530–727	PKS B1934–638	147.6
27 Aug 2011	C015	6B	2048	2048	5500	PKS B0530–727	PKS B1934–638	148.2
20 Nov 2011	C015	1.5D	2048	2048	1972,2150	PKS B0530–727	PKS B1934–638	147.6
20 Nov 2011	C015	1.5D	2048	2048	5500	PKS B0530–727	PKS B1934–638	135.6
12 Jan 2012	C015	6A	2048	2048	5500	PKS B0530–727	PKS B1934–638	450
16 Feb 2012	C015	6A	2048	2048	1972,2150	PKS B0530–727	PKS B1934–638	148.2
16 Feb 2012	C015	6A	2048	2048	5500	PKS B0530–727	PKS B1934–638	133.2
11 Apr 2012	C015	1.5B	2048	2048	1972,2150	PKS B0530–727	PKS B1934–638	118.2
11 Apr 2012	C015	1.5B	2048	2048	5500	PKS B0530–727	PKS B1934–638	118.2
06 Jun 2012	C015	6D	2048	2048	1972,2150	PKS B0530–727	PKS B1934–638	186
06 Jun 2012	C015	6D	2048	2048	5500	PKS B0530–727	PKS B1934–638	133.8
01 Sep 2012	C015	6A	2048	2048	5500	PKS B0530–727	PKS B1934–638	497.4
02 Sep 2012	C015	6D	2048	2048	1972,2150	PKS B0530–727	PKS B1934–638	147.6
02 Sep 2012	C015	6D	2048	2048	5500	PKS B0530–727	PKS B1934–638	133.2
24 Nov 2012	C015	1.5C	2048	2048	1972,2150	PKS B0530–727	PKS B1934–638	133.2
24 Nov 2012	C015	1.5C	2048	2048	5500	PKS B0530–727	PKS B1934–638	124.8
09 Dec 2012	C015	6B	2048	2048	5500	PKS B0530–727	PKS B1934–638	384
03 Jan 2013	C015	1.5D	2048	2048	1972,2150	PKS B0530–727	PKS B1934–638	200.4
03 Jan 2013	C015	1.5D	2048	2048	5500	PKS B0530–727	PKS B1934–638	192
07 Mar 2013	C015	6A	2048	2048	5500	PKS B0530–727	PKS B1934–638	482.4
03 May 2013	C015	6C	2048	2048	1972,2150	PKS B0530–727	PKS B1934–638	118.8
03 May 2013	C015	6C	2048	2048	5500	PKS B0530–727	PKS B1934–638	115.2
04 May 2013	C015	6C	2048	2048	5500	PKS B0530–727	PKS B1934–638	488.4
17 Jul 2013	C015	6A	2048	2048	5500	PKS B0530–727	PKS B1934–638	553.2
19 Jul 2013	C015	6A	2048	2048	1972,2150	PKS B0530–727	PKS B1934–638	118.2
19 Jul 2013	C015	6A	2048	2048	5500	PKS B0530–727	PKS B1934–638	117
30 Aug 2013	C015	1.5A	2048	2048	1972,2150	PKS B0530–727	PKS B1934–638	207
30 Aug 2013	C015	1.5A	2048	2048	5500	PKS B0530–727	PKS B1934–638	207.6
05 Nov 2013	C015	6A	2048	2048	5500	PKS B0530–727	PKS B1934–638	512.4
16 Apr 2014	C015	6A	2048	2048	5500	PKS B0530–727	PKS B1934–638	493.2
27 Aug 2014	C015	6B	2048	2048	5500	PKS B0530–727	PKS B1934–638	62.4
18 Oct 2014	C015	1.5A	2048	2048	5500	PKS B0530–727	PKS B1934–638	453
19 Oct 2014	C015	1.5A	2048	2048	2150	PKS B0530–727	PKS B1934–638	133.2
19 Oct 2014	C015	1.5A	2048	2048	5500	PKS B0530–727	PKS B1934–638	129.6
02 May 2015	C015	6A	2048	2048	2150	PKS B0530–727	PKS B1934–638	148.2
02 May 2015	C015	6A	2048	2048	5500	PKS B0530–727	PKS B1934–638	171.6
05 Dec 2015	C015	1.5A	2048	2048	2150	PKS B0530–727	PKS B1934–638	133.2
05 Dec 2015	C015	1.5A	2048	2048	5500	PKS B0530–727	PKS B1934–638	133.2
08 Mar 2016	C015	6B	2048	2048	2150	PKS B0530–727	PKS B1934–638	148.2
08 Mar 2016	C015	6B	2048	2048	5500	PKS B0530–727	PKS B1934–638	132.6
04 Jun 2016	C015	1.5B	2048	2048	2150	PKS B0530–727	PKS B1934–638	143.4
04 Jun 2016	C015	1.5B	2048	2048	5500	PKS B0530–727	PKS B1934–638	133.2
24 Aug 2016	C015	6C	2048	2048	2150	PKS B0530–727	PKS B1934–638	133.2
24 Aug 2016	C015	6C	2048	2048	5500	PKS B0530–727	PKS B1934–638	133.2
22 Nov 2016	C015	6A	2048	2048	2150	PKS B0530–727	PKS B1934–638	133.2
22 Nov 2016	C015	6A	2048	2048	5500	PKS B0530–727	PKS B1934–638	123.6
07 Feb 2017	C015	6D	2048	2048	5500	PKS B0530–727	PKS B1934–638	415.8
08 Feb 2017	C015	6D	2048	2048	2150	PKS B0530–727	PKS B1934–638	192
08 Feb 2017	C015	6D	2048	2048	5500	PKS B0530–727	PKS B1934–638	177.6
18 Feb 2017	C015	6D	2048	2048	2150	PKS B0530–727	PKS B1934–638	133.2
18 Feb 2017	C015	6D	2048	2048	5500	PKS B0530–727	PKS B1934–638	131.4
29 Aug 2017	C015	1.5A	2048	2048	5500	PKS B0530–727	PKS B1934–638	249
10 Nov 2017	C015	1.5C	2048	2048	5500	PKS B0530–727	PKS B1934–638	118.2
11 Nov 2017	C015	1.5C	2048	2048	5500	PKS B0530–727	PKS B1934–638	325.8
30 Dec 2017	C015	6C	2048	2048	5500	PKS B0530–727	PKS B1934–638	508.2

Table 2: Details of *Chandra* X-ray observations.

Obs. ID	Date	PI	Exp. time (ks)
1967	2000-12-07	R. McCray	98.76
2831	2001-12-12	D. Burrows	49.41
2832	2002-05-15	D. Burrows	44.26
3829	2002-12-31	D. Burrows	49.01
3830	2003-07-08	D. Burrows	45.31
4614	2004-01-02	D. Burrows	46.49
4615	2004-07-22	D. Burrows	48.83

et al. 2020). If our interpretation is correct, the Honeycomb Nebula exploded inside a low-density wind cavity. To test this scenario, we need further H α observations with finer angular resolution.

3.6. X-ray emission

Our three-colour Chandra image of the Honeycomb Nebula is shown in Fig. 4. As shown in Fig. 5(c), its morphology is broadly similar to the radio morphology of our new ATCA images, with its brightness increasing towards the western side where the SNR is thought to be evolving into a denser ambient medium. However, as noted above, on small scales the X-ray and radio emission are not well correlated, which is expected given their thermal and non-thermal origins, respectively.

Table 3: Flux density measurements of the Honeycomb Nebula.

Frequency (MHz)	Flux (Jy)	Flux error (Jy)	Telescope	Reference
888	0.181	0.0181	ASKAP	Pennock et al. (2021)
2000	0.110	0.0220	ATCA	This work
5500	0.046	0.0089	ATCA	This work

Maggi et al. (2016) performed an X-ray spectral analysis of the Honeycomb Nebula using *XMM-Newton* data, finding that its emission is soft with a plasma temperature (kT) of ~ 0.3 keV and faint with an X-ray luminosity (L_X) of $\sim 4 \times 10^{34}$ erg s $^{-1}$ in the 0.3–8 keV range. In addition, the spectra showed enhanced abundances of α -process elements, which along with the star formation history in the region led to Maggi et al. (2016) assigning a high probability that the Honeycomb Nebula resulted from a core-collapse event.

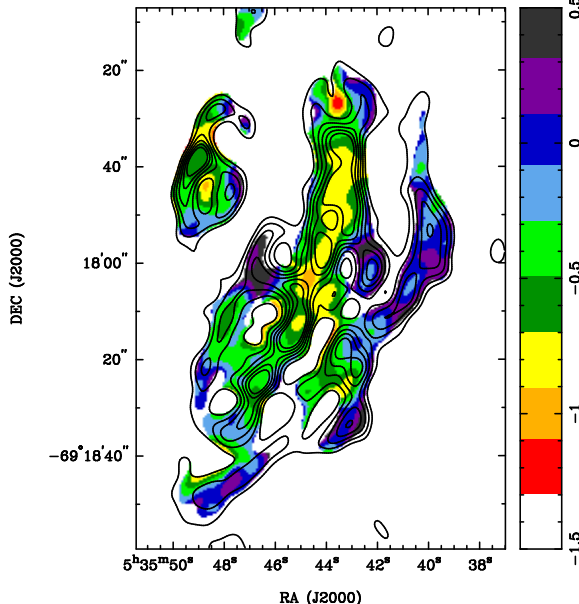


Fig. 7: Spectral index map of the Honeycomb Nebula (ATCA; 2000, 5500 MHz) with 5500 MHz contour lines overlaid. The contour levels are 0.00005, 0.0001, 0.00015, 0.0002, 0.00025 and 0.0003 Jy beam $^{-1}$. The colour bar on the right-hand side represent gradients of spectral index.

Given the small size of the nebula and assuming size is a useful proxy for age, the relatively low observed luminosity and temperature are unusual. Another example of such an SNR is MCSNR J0512–6707 reported by Kavanagh et al. (2015), which is slightly larger than the Honeycomb Nebula though somewhat cooler and fainter. These authors suggest that MCSNR J0512–6707 initially evolved into the wind-blown cavity of the progenitor and is now in-

teracting with the swept-up shell. If the Honeycomb Nebula resulted from a similar interaction, as we suggest above, the low kT and L_X observed further support this interpretation.

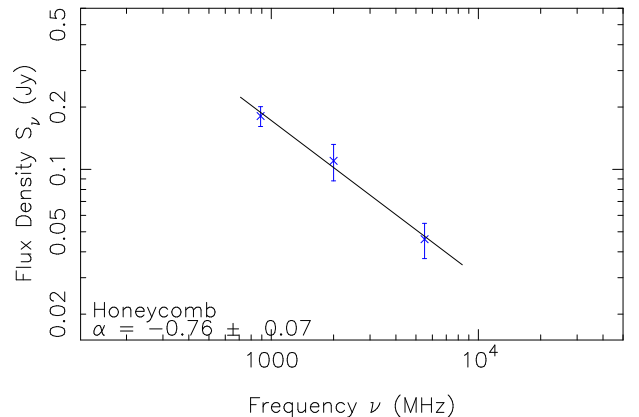


Fig. 8: Radio continuum spectrum of the Honeycomb Nebula.

3.7. The Honeycomb SNR surface brightness

We compared a previous Σ –D diagram (Urošević 2022, 2020, Pavlović et al. 2018, their Fig. 3) with our values, $D = 17.7$ pc and $\Sigma_{1\text{GHz}} = 30 \times 10^{-20} \text{ W m}^{-2} \text{ Hz}^{-1} \text{ sr}^{-1}$, for the Honeycomb Nebula. From this comparison, we believe that the Honeycomb Nebula is undergoing expansion within a surrounding environment characterised by a low density of $0.02\text{--}0.2 \text{ cm}^{-3}$ (Fig. 9).

We should emphasise that scatter of evolutionary tracks in Σ – D plane is obvious. It is a result of SNR evolution in different environments with different explosion energies. The Honeycomb nebula is indeed close to the 0.2 cm^{-3} and 10^{51} erg track, at the brightness maximum which marks the transition between free expansion and Sedov's phase. However, Pavlović et al. (2018) models are basically for SN Ia (uniform medium), and only for certain SN II models they assume a circumstellar medium with power-law density profile r^{-2} . If this SNR is expanding in a cavity, then we would have an approximately homogeneous density until the transition to ISM where, probably, would be a dense shell (or shells). Due to this, the evolutionary status established here should be taken with caution.

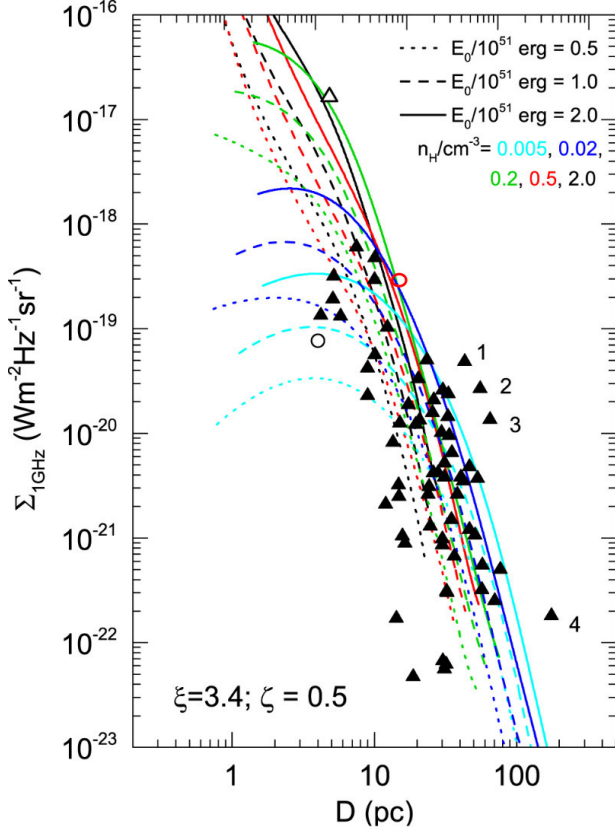


Fig. 9: Radio surface brightness-to-diameter diagram for SNRs at frequency of 1 GHz (black triangles), obtained from numerical simulations (Pavlović *et al.* 2018, their Fig. 3). The Honeycomb Nebula is marked with open red circle while the open triangle represents Cassiopeia A. The open circle represents the youngest Galactic SNR, G1.9+0.3 (Luken *et al.* 2020). Numbers represent the following SNRs: (1) CTB 37A, (2) Kes 97, (3) CTB 37B and (4) G65.1+0.6.

4. CONCLUSIONS

We present new high-resolution and sensitive ATCA images for the LMC Honeycomb Nebula at 2000 and 5500 MHz. We also compare these images with the available X-ray, optical and HI images.

The following is a summary of our findings:

- The Honeycomb Nebula has a steeper than average SNR radio spectral index of -0.76 ± 0.07 , suggesting a younger age,
- A radial polarisation with an average fractional polarisation of $24 \pm 5\%$ and maximum value of $95 \pm 16\%$ at 5500 MHz, also indicating a younger age,
- An eqp field of $48 \pm 5 \mu\text{G}$, also is consistent with a younger age,
- This SNR has the highest surface brightness, $\Sigma_{1\text{GHz}} = 30 \times 10^{-20} \text{ W m}^{-2} \text{ Hz}^{-1} \text{ sr}^{-1}$ for its

diameter in comparison to Galactic SNRs presented in Fig. 9. It tentatively suggests a previous expansion in a homogeneous low-density medium and, after that, collision with a denser shell of a young SNR in the transition between the late free expansion and early Sedov phase of evolution.

When combined with its unusual morphology and other data found in the literature, this all indicates that the remnant's progenitor most likely underwent a core-collapse event inside a low-density wind cavity.

Acknowledgements – The Australia Telescope Compact Array (ATCA) and Australian SKA Pathfinder (ASKAP) are part of the Australia Telescope National Facility which is managed by CSIRO. H.S. acknowledges funding from JSPS KAKENHI Grant Number 21H01136. D.U. acknowledges the Ministry of Education, Science and Technological Development of the Republic of Serbia support through the contract No. 451-03-66/2024-03/200104, and the support through the joint project of the Serbian Academy of Sciences and Arts and Bulgarian Academy of Sciences on the detection of extragalactic SNRs and HII regions.

REFERENCES

- Alsaberi, R. Z. E., Maitra, C., Filipović, M. D., et al. 2019, *MNRAS*, **486**, 2507
 Arbutina, B., Urošević, D., Andjelić, M. M., Pavlović, M. Z. and Vukotić, B. 2012, *ApJ*, **746**, 79
 Arbutina, B., Urošević, D., Vučetić, M. M., Pavlović, M. Z. and Vukotić, B. 2013, *ApJ*, **777**, 31
 Bertin, E., Mellier, Y., Radovich, M., et al. 2002, in Astronomical Society of the Pacific Conference Series, Vol. 281, Astronomical Data Analysis Software and Systems XI, ed. D. A. Bohlender, D. Durand, and T. H. Hanley, 228
 Bozzetto, L. M., Filipović, M. D., Vukotić, B., et al. 2017, *ApJS*, **230**, 2
 Bozzetto, L. M., Filipović, M. D., Sano, H., et al. 2023, *MNRAS*, **518**, 2574
 Chu, Y.-H., Dickel, J. R., Staveley-Smith, L., Osterberg, J. and Smith, R. C. 1995, *AJ*, **109**, 1729
 Cotton, W. D., Filipović, M. D., Camilo, F., et al. 2024, *MNRAS*, **529**, 2443
 Crawford, E. J., Filipović, M. D., McEntaffer, R. L., et al. 2014, *AJ*, **148**, 99
 Filipović, M. D. and Tothill, N. F. H., eds. 2021, Multimessenger Astronomy in Practice, 2514-3433 (IOP Publishing)
 Filipović, M. D., Payne, J. L., Reid, W., et al. 2005, *MNRAS*, **364**, 217
 Filipović, M. D., Haberl, F., Winkler, P. F., et al. 2008, *A&A*, **485**, 63
 Filipović, M. D., Payne, J. L., Alsaberi, R. Z. E., et al. 2022, *MNRAS*, **512**, 265

- Fruscione, A., McDowell, J. C., Allen, G. E., et al. 2006, in Society of Photo-Optical Instrumentation Engineers (SPIE) Conference Series, Vol. 6270, Society of Photo-Optical Instrumentation Engineers (SPIE) Conference Series
- Galvin, T. J. and Filipovic, M. D. 2014, *SerAJ*, **189**, 15
- Garmire, G. P., Bautz, M. W., Ford, P. G., Nousek, J. A. and Ricker, Jr., G. R. 2003, in Society of Photo-Optical Instrumentation Engineers (SPIE) Conference Series, Vol. 4851, X-Ray and Gamma-Ray Telescopes and Instruments for Astronomy., ed. J. E. Truemper and H. D. Tananbaum, 28–44
- Gooch, R. 1995, in Astronomical Society of the Pacific Conference Series, Vol. 77, Astronomical Data Analysis Software and Systems IV, ed. R. A. Shaw, H. E. Payne, and J. J. E. Hayes, 144
- Gvaramadze, V. V., Kniazev, A. Y. and Oskinova, L. M. 2019, *MNRAS*, **485**, L6
- Haberl, F., Sturm, R., Ballet, J., et al. 2012, *A&A*, **545**, A128
- Joseph, T. D., Filipović, M. D., Crawford, E. J., et al. 2019, *MNRAS*, **490**, 1202
- Joye, W. A. and Mandel, E. 2003, in Astronomical Society of the Pacific Conference Series, Vol. 295, Astronomical Data Analysis Software and Systems XII, ed. H. E. Payne, R. I. Jedrzejewski, and R. N. Hook, 489
- Kavanagh, P. J., Sasaki, M., Bozzetto, L. M., et al. 2015, *A&A*, **583**, A121
- Kim, S., Staveley-Smith, L., Dopita, M. A., et al. 2003, *ApJS*, **148**, 473
- Luken, K. J., Filipović, M. D., Maxted, N. I., et al. 2020, *MNRAS*, **492**, 2606
- Macri, L. M., Stanek, K. Z., Bersier, D., Greenhill, L. J. and Reid, M. J. 2006, *ApJ*, **652**, 1133
- Maggi, P., Haberl, F., Kavanagh, P. J., et al. 2016, *A&A*, **585**, A162
- Maggi, P., Filipović, M. D., Vukotić, B., et al. 2019, *A&A*, **631**, A127
- Meaburn, J., Wang, L., Palmer, J., and Lopez, J. A. 1993, *MNRAS*, **263**, L6
- Meaburn, J., Redman, M. P., Boumis, P. and Harvey, E. 2010, *MNRAS*, **408**, 1249
- Owen, R. A., Filipović, M. D., Ballet, J., et al. 2011, *A&A*, **530**, A132
- Pavlović, M. Z., Urošević, D., Arbutina, B., et al. 2018, *ApJ*, **852**, 84
- Payne, J. L., White, G. L., Filipović, M. D. and Pannuti, T. G. 2007, *MNRAS*, **376**, 1793
- Pennock, C. M., van Loon, J. T., Filipović, M. D., et al. 2021, *MNRAS*, **506**, 3540
- Pietrzyński, G., Graczyk, D., Gallenne, A., et al. 2019, *Natur*, **567**, 200
- Redman, M. P., Al-Mostafa, Z. A., Meaburn, J., Bryce, M. and Dyson, J. E. 1999, *A&A*, **345**, 943
- Reynolds, S. P., Gaensler, B. M. and Bocchino, F. 2012, *SSRv*, **166**, 231
- Roper, Q., McEntaffer, R. L., DeRoo, C., et al. 2015, *ApJ*, **803**, 106
- Sano, H., Matsumura, H., Yamane, Y., et al. 2019, *ApJ*, **881**, 85
- Sano, H., Plucinsky, P. P., Bamba, A., et al. 2020, *ApJ*, **902**, 53
- Sault, R. J., Teuben, P. J. and Wright, M. C. H. 1995, in Astronomical Society of the Pacific Conference Series, Vol. 77, Astronomical Data Analysis Software and Systems IV, ed. R. A. Shaw, H. E. Payne, and J. J. E. Hayes, 433
- Urošević, D. 2014, *Ap&SS*, **354**, 541
- Urošević, D. 2020, *NatAs*, **4**, 910
- Urošević, D. 2022, *PASP*, **134**, 061001
- Urošević, D., Pavlović, M. Z. and Arbutina, B. 2018, *ApJ*, **855**, 59
- van der Marel, R. P. and Cioni, M.-R. L. 2001, *AJ*, **122**, 1807
- Wang, L. 1992, *Msngr*, **69**, 34
- Weisskopf, M. C., O'dell, S. L. and van Speybroeck, L. P. 1996, in Society of Photo-Optical Instrumentation Engineers (SPIE) Conference Series, Vol. 2805, Multi-layer and Grazing Incidence X-Ray/EUV Optics III, ed. R. B. Hoover and A. B. Walker, 2–7
- Yew, M., Filipović, M. D., Stupar, M., et al. 2021, *MNRAS*, **500**, 2336

ИСТРАЖИВАЊЕ ОСТАТКА СУПЕРНОВЕ У РАДИО-КОНТИНУУМУ – МАГЛИНА САЋЕ (HONEYCOMB) ИЗ ВЕЛИКОГ МАГЕЛНОВОГ ОБЛАКА

R. Z. E. Alsaberi¹ , M. D. Filipović¹ , H. Sano^{2,3} , P. Kavanagh⁴ , P. Janas⁴ ,
J. L. Payne¹  и Д. Урошевић⁵ 

¹ Western Sydney University, Locked Bag 1797, Penrith South DC, NSW 1797, Australia

E-mail: 19158264@student.westernsydney.edu.au

² Faculty of Engineering, Gifu University, 1-1 Yanagido, Gifu 501-1193, Japan

³ Center for Space Research and Utilization Promotion (c-SRUP), Gifu University,
1-1 Yanagido, Gifu 501-1193, Japan

⁴ Department of Experimental Physics, Maynooth University, Maynooth, Co. Kildare, Ireland

⁵ Катедра за астрономију, Математички факултет, Универзитет у Београду,
Студентски трг 16, 11000 Београд, Србија

УДК 52–13–77 : 524.722.3

Оригинални научни рад

У овом раду приказујемо прва дубинска архивска посматрања остатка супернове маглине Саће (Honeycomb), из Великог Магелановог облака, телескопом ATCA (Australia Telescope Compact Array) у радио-континууму. Ова радио-посматрања су рађена на 2000 и 5500 MHz. Пронашли смо да је радио-спектрални индекс овог остатка -0.76 ± 0.07 а просечна поларизација $25 \pm 5\%$ са максималном од $95 \pm 16\%$. Израчунали смо да је еквипартијско магнетно поље овог остатка $48 \pm 5 \mu G$, а ми-

нимална енергија $E_{\min} = 3 \times 10^{49}$ erg. Површински сјај маглине Саће на $\Sigma_{1\text{GHz}}$ је 30×10^{-20} W m $^{-2}$ Hz $^{-1}$ sr $^{-1}$. Користећи $\Sigma - D$ релацију нашли смо да се остатак шири у средини са ниском густином. Наша HI посматрања потврђују идеју да се маглина Саће шири унутар ниско-густинског међура створеног ветром са звезде прогенитора. Највероватније, овај остатак се налази у еволутивној фази између краја фазе слободног ширења и ране Седовљеве фазе.